Wind and Structures, Vol. 12, No. 6 (2009) 479-504
DOI: http://dx.doi.org/10.12989/was.2009.12.6.479

Buffeting-induced stresses in a long suspension bridge: structural health monitoring oriented stress analysis

T.T. Liu[1,2], Y.L. Xu[2,*], W.S. Zhang[1,2], K.Y. Wong[3], H.J. Zhou[2] and K.W.Y. Chan[3]

[1]*Department of Engineering Mechanics, Dalian University of Technology, Dalian, China*
[2]*Department of Civil and Structural Engineering,*
The Hong Kong Polytechnic University, Hung Hom, Kowloon, Hong Kong
[3]*Bridges and Structures Division, Highways Department,*
The Government of Hong Kong Special Administrative Region, Hong Kong

(Received August 20, 2007, Accepted June 22, 2009)

Abstract. Structural health monitoring (SHM) systems have been recently embraced in long span cable-supported bridges, in which buffeting-induced stress monitoring is one of the tasks to ensure the safety of the bridge under strong winds. In line with this task, this paper presents a SHM-oriented finite element model (FEM) for the Tsing Ma suspension bridge in Hong Kong so that stresses/strains in important bridge components can be directly computed and compared with measured ones. A numerical procedure for buffeting induced stress analysis of the bridge based on the established FEM is then presented. Significant improvements of the present procedure are that the effects of the spatial distribution of both buffeting forces and self-excited forces on the bridge deck structure are taken into account and the local structural behaviour linked to strain/stress, which is prone to cause local damage, are estimated directly. The field measurement data including wind, acceleration and stress recorded by the wind and structural health monitoring system (WASHMS) installed on the bridge during Typhoon York are analyzed and compared with the numerical results. The results show that the proposed procedure has advantages over the typical equivalent beam finite element models.

Keywords: suspension bridge; finite element model; buffeting; stress analysis; structural health monitoring; comparison.

1. Introduction

With increasing span length, modern long suspension bridges become more and more flexible and susceptible to strong winds. This leads to a significant increase of buffeting response of the bridges, which in turn may result in a substantial increase in stresses and fatigue damage to structural components and connections (Li, *et al.* 2002). Therefore, an accurate prediction of buffeting response including buffeting–induced stresses of the bridges becomes imperative.

Most of the existing buffeting analysis methods are based on the aerodynamic strip theory and the quasi-steady linear theory (Davenport 1962, Scanlan and Gade 1977, Lin and Yang 1983), and they are actually a combination of numerical, experimental, and analytical approaches. Finite element

* Chair Professor, Corresponding Author, E-mail: ceylxu@polyu.edu.hk

technique is often used to model a bridge deck using 3D equivalent beam finite elements. Wind tunnel tests of bridge section models provide flutter derivatives and aerodynamic coefficients. Buffeting response of the bridge deck is then determined either in the frequency domain based on random vibration theory or in the time domain through simulation (Jain, *et al*. 1996, Chen, *et al*. 2000, Xu, *et al.* 2000, Liu, *et al.* 2004). Nevertheless, the modelling of a complex bridge deck using equivalent beam finite elements may oversimplify the problem. The ignorance of spatial distribution of both buffeting forces and self-excited forces across the cross section of the bridge deck may have a considerable impact on the accuracy of the buffeting-induced stress responses. There is also an increasing trend to install structural health monitoring (SHM) systems in long suspension bridges to monitor the safety and functionality of the bridges at both global and stress levels (Wong 2004, Chan, *et al.* 2005). The currently-used buffeting analysis methods should be improved to accommodate structural health monitoring oriented stress analysis.

In line with this task, this paper presents a structural health monitoring oriented finite element model (FEM) for the Tsing Ma suspension bridge in Hong Kong so that stresses/strains in important bridge components can be directly computed and compared with measured ones. A numerical procedure for buffeting induced stress analysis of the bridge based on the established FEM is then presented. Local strains and stresses in structural members of the bridge deck, which are prone to cause local damage, are predicted directly using the mode superposition technique in the time domain. The field measurement data including wind, acceleration and stress recorded by the anemometers, accelerometers, and strain gauges in the Wind and Structural Health Monitoring System (WASHMS) installed on the bridge during Typhoon York are analyzed and compared with the numerical results to verify, to some extent, the proposed stress analysis procedure. Once the proposed procedure is confirmed, it can be used to predict buffeting stresses and their distributions in the locations where no sensors are installed. As a result, a complete structural health monitoring oriented stress analysis can be performed and the stress-related safety of the bridge can be evaluated.

2. Structural health monitoring oriented finite element model

2.1. Main features of Tsing Ma Bridge

The Tsing Ma Bridge, stretching from the Tsing Yi Island to the Ma Wan Island, is a suspension bridge with a main span of 1,377 m that carries a dual three-lane highway on the upper level of the bridge deck and two railway tracks and two carriageways on the lower level within the bridge deck, as shown in Fig. 1 (Xu, *et al.* 1997). The height of the towers is 206 m, measured from the base

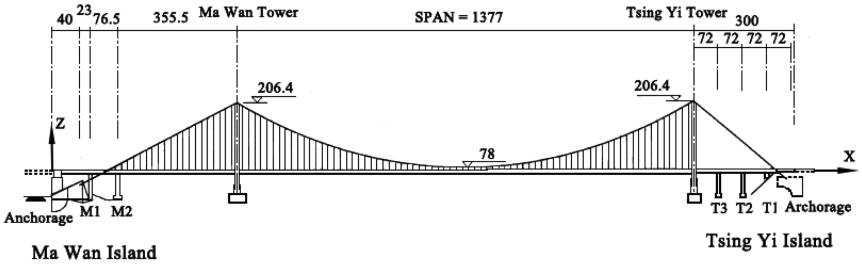

Fig. 1 Configuration of Tsing Ma Bridge (unit:m)

level to the tower saddle. The two main cables of 36 m apart in the north and south are accommodated by the four saddles located at the top of the tower legs in the main span. On the Tsing Yi side, the main cables are extended from the tower saddles to the main anchorage through the splay saddles, forming a 300 m Tsing Yi side span. On the Ma Wan side, the main cables extended from the Ma Wan tower are held first by the saddles on Pier M2 at a horizontal distance of 355.5 m from the Ma Wan tower and then by the main anchorage through splay saddles at the Ma Wan abutment. The bridge deck is a hybrid steel structure continuing between the two main anchorages.

2.2. Finite element modelling of Tsing Ma Bridge

Modelling work is executed using the commercial software packages MSC/PATRAN as model builder and MSC/NASTRAN as finite element solver. The modelling work is based on the previous model developed by the fourth author (Wong 2002) with the following principles: (1) model geometry should accurately represent actual geometry; (2) one analytical member should represent one real member; (3)stiffness and mass should be simulated and quantified properly; (4) boundary and continuity conditions should accurately represent reality; and (5) the model should be detailed enough at both global and local levels to facilitate subsequent model updating and buffeting-induced stress analysis.

The deck is a hybrid steel structure consisting of Vierendeel cross-frames supported on two longitudinal trusses acting compositely with stiffened steel plates that carry the upper and lower highways. The bridge deck at the main span is a suspended deck and the structural configuration is typical for every 18 m segment. Fig. 2(a) illustrates a typical 18 m suspended deck module consisting of mainly longitudinal trusses, cross frames, highway decks, railway tracks, and bracings. The upper and lower chords of the longitudinal trusses are of box section while the vertical and diagonal members of the longitudinal trusses are of I-section. They are all modelled as 12-DOF beam elements (CBAR) based on the principle of one element for one member. The upper and lower chords of the cross frames are of T-section dominantly except for some segments with I-section for the cross bracing systems. The inner struts, outer struts, and upper and lower inclined edge members of the cross frames all are of I-section. All the members in the cross frames are modelled as 12-DOF beam elements (CBAR) with actual section properties except for the edge members which are assigned large elastic modulus and significantly small density to reflect the real situation where the joint is heavily stiffened for the connection with the suspender. All the members in the cross bracings are of box–section while all the members in the sway bracings are of circular hollow section. These members all are modelled as 12-DOF beam elements (CBAR) with actual section properties. Each railway track is modelled as an equivalent beam modelled by special 14-DOF beam elements (CBEAM) which are similar to the elements (CBAR) but with additional properties such as variable cross-section, shear centre offset from the neutral axis, wrap coefficient and others. The railway tracks are meshed every 4.5 m according to the interval of the adjacent cross frames. The modulus of elasticity, the density and Poisson's ratio for all members, except for the edge members, are taken as 2.05×10^{11} N/m^2, 8,500 kg/m^3 and 0.3, respectively. Deck plates and deck troughs comprise orthotropic decks, and the accurate modelling of stiffened deck plates is complicated. To keep the problem manageable, two-dimensional anisotropic quadrilateral plate-bending elements (CQUAD4) are employed to model the stiffened deck plates. The equivalent section properties of the elements are estimated roughly by a static analysis and the material

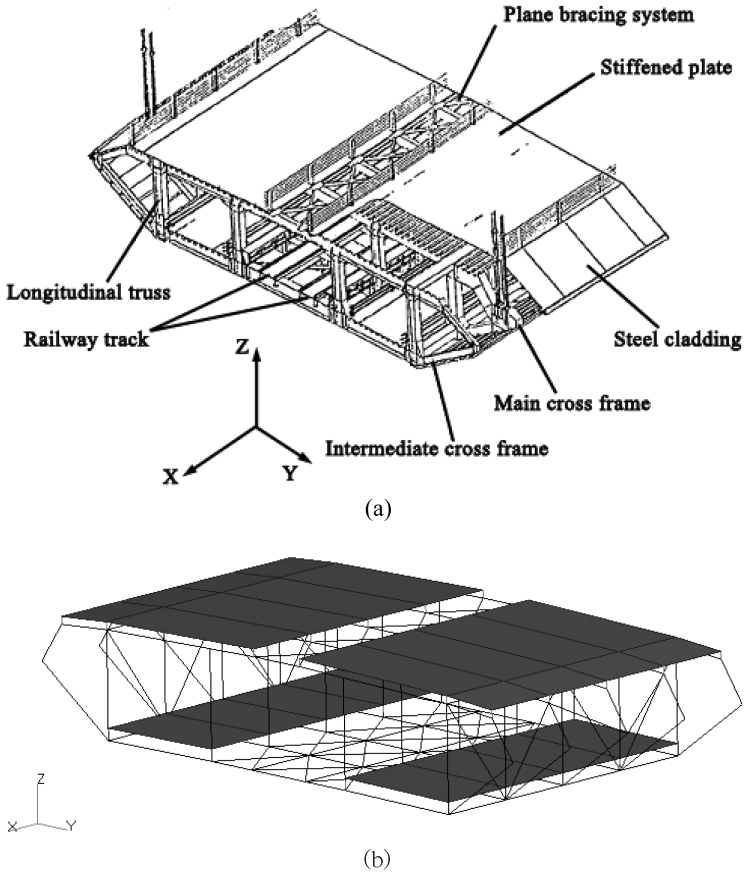

Fig. 2 A typical 18-m deck section at the main span: a) An isometric view of a typical deck section; b) FE model of an 18-m deck section

properties of steel are used first but it is updated subsequently. The connections between the deck plates and the chords of the cross frames and the longitudinal trusses involve the use of MPC (Multi-Point Connection). Proper offsets of neutral axes for the connections between the components are considered to maintain the original configuration. In the modelling of the concerned typical 18-m deck module, a total of 130 nodes with 172 CBAR elements, 16 CBEAM elements, 24 CQUAD4 elements and 50 MPCs are used. The skeleton view of the 3-D finite element model of the 18-m deck module is shown in Fig. 2(b). The deck modules at the Ma Wan tower, at the Ma Wan approach span, at the Tsing Yi tower and at the Tsing Yi approach span are constructed using the same principle as the deck module at the main span while considering the differences in the shape and size of cross frames, longitudinal trusses and other members.

The Ma Wan tower and the Tsing Yi tower are reinforced concrete structures, and each tower consists of two reinforced concrete legs which are linked by four reinforced concrete portal beams. The bridge towers are represented by multilevel portal frames in this study. The tower legs are modelled using 12-DOF beam elements (CBAR). The tower leg from its foundation to the deck level is meshed with the element of a length of 5 m. At the deck level, the tower leg is meshed according to the positions of the lateral bearings. Though the dimension of the cross section of the

tower leg varies from its bottom to its top, the geometric properties of the beam element are assumed to be constant along its axis with an average value based on the design drawings. The four portal beams of either tower are also modelled using CBAR elements but with different section geometric properties. The deck-level portal beam of each tower is divided at the four particular positions, which correspond to the four vertical bearings between the bridge deck and the tower. The mass density, the Poisson's ratio and the modulus of elasticity of reinforced concrete for the towers are estimated to be 2,500 kg/m^3, 0.2 and 3.4×10^{10} N/m^2, respectively.

The two side spans on the Ma Wan side and Tsing Yi side are supported by two and three piers, respectively. All supporting piers in the side spans are reinforced concrete structures. Piers M1, T2, and T3 are similarly modelled as a portal frame using 12-DOF beam elements (CBAR). Pier M2 is also modelled as a portal frame using 12 CBAR elements, in which the upper portal beam is meshed according to the four vertical bearing positions. The wall panel of pier T1 is represented by an equivalent portal frame with 25 CBAR elements. The mass density, the Poisson's ratio and the modulus of elasticity of reinforced concrete for the piers are taken as 2,500 kg/m^3, 0.2 and 3.4×10^{10} N/m^2, respectively.

The cable system is the major system supporting the bridge deck. The cable system consists of two main cables, 95 pairs of suspender units and 95 pairs of cable bands. CBEAM elements are used to model the main cables. The cable between the adjacent suspender units is modelled by one beam element of a circular cross section. The DOFs for the rotational displacements of each beam element are released at both ends because the cable is considered to be capable of resisting tensile force only. 77 beam elements are used to model each cable in the main span while 26 and 8 elements are used to model one cable on the Ma Wan side span and on the Tsing Yi side span respectively. Each suspender unit is modelled by one CBEAM element to represent the four strands. A total of 190 elements are used to model all the suspender units. Since this study does not concern the stress distribution around the connection between the main cable and suspenders, the modelling of cable bands is ignored in the global bridge model. The connections between the main cables and suspenders are achieved by simply sharing their common nodes. To model the cable system, the geometry of cable profile should be determined. The geometric modelling of the two parallel main cables follows the profiles of the cables under the design dead load at a design temperature 23ºC based on the information from the design drawings. The horizontal tension in the main cable from pier M2 to the Ma Wan anchorage is 400,013 kN but it is 405,838 kN in the other parts of the main cable. The tension forces in the suspenders on the Ma Wan side span are taken as 2,610 kN but they are 4,060 kN in the other suspenders. The mass densities for both cables and suspenders are taken as 8,200 kg/m^3. The area of cross section is 0.759 m^2 for the main cables and 0.018 m^2 for the suspenders. The modulus of elasticity is greatly influenced by the tension in the main cables and suspenders, which is estimated as 1.95×10^{11} N/m^2 and 1.34×10^{11} N/m^2 respectively at design temperature of 23ºC and will be updated subsequently.

By integrating the bridge components with the proper modelling of the connections and boundary conditions, the entire global bridge mode is established as shown in Fig. 3. The establishment of this global bridge model involves 12,898 nodes, 21,946 elements (2906 plate elements and 19040 beam elements) and 4788 MPCs. Although the geometric features and supports of bridge deck have been modelled in a great detail in the established 3-D finite element model of the Tsing Ma Bridge, the modelling discrepancies from the as-built bridge still exist. The modelling discrepancies mainly come from four sources: (1) the simplified modelling of stiffened plates; (2) the uncertainties in pavement mass and others; (3) the uncertainties in the stiffness of bearings; and (4) the rigid

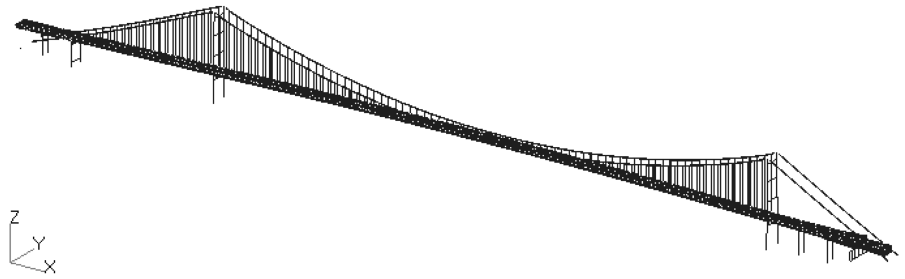

Fig. 3 3-D Finite element model of Tsing Ma Bridge

connection assumption. The model updating is therefore necessary. In this regard, the objective function representing the differences between the analytical and measured natural frequencies is minimized. The measured first 18 natural frequencies and mode shapes of the bridge (Xu, *et al.* 1997) are used in the model updating (Zhang, *et al.* 2007). The correlation of computed mode shapes with measured ones is evaluated using modal assurance criterion. It turns out that the updated complex FE model could provide comparable and credible structural dynamic modal characteristics. Further details can be found in Zhang, *et al.* (2007).

3. Formulation

3.1. Equation of motion

The governing equation of motion with respect to the static equilibrium position of the bridge based on the SHM oriented finite element model in the presence of buffeting forces and self-excited forces can be expressed as:

$$\mathbf{M}\ddot{\mathbf{X}}(t) + \mathbf{C}\dot{\mathbf{X}}(t) + \mathbf{K}\mathbf{X}(t) = \mathbf{F}^{bf} + \mathbf{F}^{se} \tag{1}$$

where, **M**, **C** and **K** are the global structural mass, damping and stiffness matrices of the bridge with the dimensions of $6N \times 6N$, in which N is the total number of nodes in the FEM; $\mathbf{X}(t) = \{\mathbf{X}_1(t), \mathbf{X}_2(t), \cdots, \mathbf{X}_N(t)\}^T$ is the nodal displacement vector of the bridge and $\mathbf{X}_j(t)$ is the *6x1* displacement vector of the jth node in the global coordinate system with the first three being translational displacements and the last three being rational displacements; each over-dot denotes one order of partial differentiation with respect to time; $\mathbf{F}^{bf}$ and $\mathbf{F}^{se}$ are the corresponding nodal buffeting force vector and self-excited force vector, respectively.

3.2. Buffeting forces

Most of the buffeting analysis methods are based on the aerodynamic strip theory and the quasi-steady theory. A bridge deck is often modelled using 3D equivalent beam finite elements. Buffeting forces and self-excited forces act at the centre of elasticity of the deck section. By assuming no interaction between buffeting forces and self-excited forces, the equivalent buffeting forces acting at the centre of elasticity of the deck segment of unit length are expressed as

$$\mathbf{F}_{ei}^{bf} = \mathbf{A}_{ei}^{bf}\mathbf{q}_i \tag{2}$$

in which

$$\mathbf{F}_{ei}^{bf} = \begin{Bmatrix} D_{ei}^{bf} \\ L_{ei}^{bf} \\ M_{ei}^{bf} \end{Bmatrix}; \quad \mathbf{q}_i = \begin{Bmatrix} u_i \\ w_i \end{Bmatrix}; \quad \mathbf{A}_{ei}^{bf} = \frac{1}{2}\rho U_i^2 B_i L_i \begin{bmatrix} \chi_{D_{bu}}\left(\frac{2C_{Di}}{U_i}\right) & \chi_{D_{bw}}\left(\frac{C'_{Di}}{U_i}\right) \\ \chi_{L_{bu}}\left(\frac{2C_{Li}}{U_i}\right) & \chi_{L_{bw}}\left(\frac{C'_{Li}+C_{Di}}{U_i}\right) \\ \chi_{M_{bu}}\left(\frac{2C_{Mi}}{U_i}\right)B_i & \chi_{M_{bw}}\left(\frac{C'_{Mi}}{U_i}\right)B_i \end{bmatrix} \tag{3}$$

where D_{ei}^{bf}, M_{ei}^{bf}, L_{ei}^{bf} are the equivalent buffeting drag, moment, and lift, respectively, on the ith node of the equivalent bridge deck beam (see Fig. 4); ρ is the air density; U_i is the mean velocity of the incident wind perpendicular to the ith deck segment; B_i and L_i are the width and length of the bridge deck segment at the ith node, respectively; C_{Di}, C_{Li}, C_{Mi} are the drag, lift, and moment coefficients, respectively, of the ith bridge deck segment; $C'_{Di} = dC_{Di}/da$; $C'_{Li} = dC_{Li}/da$; $C'_{Mi} = dC_{Mi}/da$; α is the angle of attack of normal incident wind referring to the horizontal plane of the deck; $u_i(t)$ and $w_i(t)$ are the horizontal and vertical components of fluctuating wind, respectively; and $\chi_{D_{bu}}$, $\chi_{D_{bw}}$, $\chi_{M_{bu}}$, $\chi_{M_{bw}}$, $\chi_{L_{bu}}$, $\chi_{L_{bw}}$ are the aerodynamic transfer functions between fluctuating wind velocities and buffeting forces.

In reality, the equivalent buffeting forces are actually associated with the spatial distribution of wind pressures on the surface of the bridge deck, as shown in Fig. 5. The ignorance of spatial distribution and/or aerodynamic transfer function of buffeting forces across the cross section of the bridge deck may have a considerable impact on the accuracy of buffeting response prediction. Furthermore, local structural behaviour of the bridge deck associated with local stress and strain, which is prone to cause local damage, could not be predicted directly by the currently-used approaches based on the equivalent buffeting forces. Therefore, the currently-used buffeting analysis methods should be improved to accommodate SHM oriented stress analysis. Let us assume that

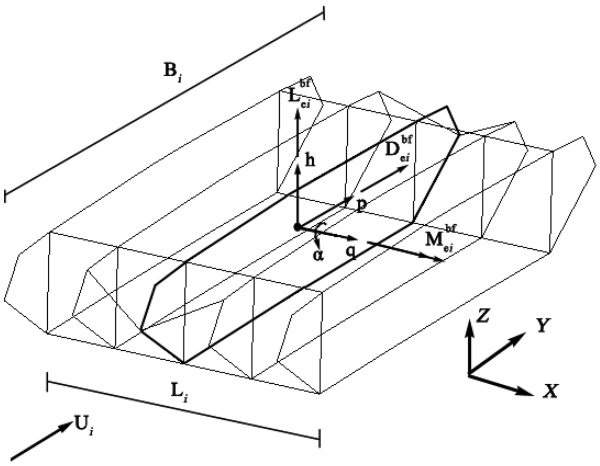

Fig. 4 Buffeting forces at the centre of elasticity of the ith deck section

wind pressure distribution on the surface of the ith section of the bridge deck can be measured at any given time through wind tunnel tests or field measurements. The buffeting forces at the kth node due to wind pressures acting on the jth element of the ith section of the bridge deck (see Fig. 5) can be obtained by

$$\{F_{k-1}(t), F_k(t)\}_{ji} = \left\{ \int_0^{l_{ji}} (1 - s/l_{ji}) p_{ji}(s,t) ds, \int_0^{l_{ji}} (s/l_{ji}) p_{ji}(s,t) ds \right\} \tag{4}$$

in which l_{ji} is the length of jth element in the ith section ($j = 1,2,\cdots,N_{si}$); N_{si} is the number of elements used to model the ith deck section; $p_{ji}(s,t)$ is wind pressure distribution over the jth element; s is the local element coordinate; $\{F_{k-1}(t),F_k(t)\}_{ji}$ are the buffeting forces at the (k-1)th and kth nodes, respectively, in the local coordinate of the jth element. The buffeting force $\{F_k(t)\}_{ji}$ at the kth node of the jth element in the local coordinate can then be converted to $\{F_{ky},F_{kz}\}_{ji}$ in the p-h-q coordinate system or the x-y-z global coordinate system (see Fig. 5). Finally, by adding the buffeting forces at the kth node from all the connecting elements together, the buffeting force vector at the kth node in the ith deck section in the global coordinate system can be obtained as $\mathbf{F}_{ki}^{bf} = \{0, F_{kiy}^{bf}, F_{kiz}^{bf}, 0, 0, 0\}^T$, in which $k = 1,2,\cdots,N_{di}$ and N_{di} is the number of nodes used to model the ith deck section. After this procedure is applied to all the nodes in all the sections of the SHM oriented finite element model of the bridge, the buffeting force vector in Eq. (1) can be formed.

Nevertheless, it is almost impossible in practice to obtain fluctuating wind pressure distribution for the whole bridge deck as a function of time. Fluctuating wind pressure distribution on a typical bridge deck section may not be available in most of cases, such as Tsing Ma Bridge used in this

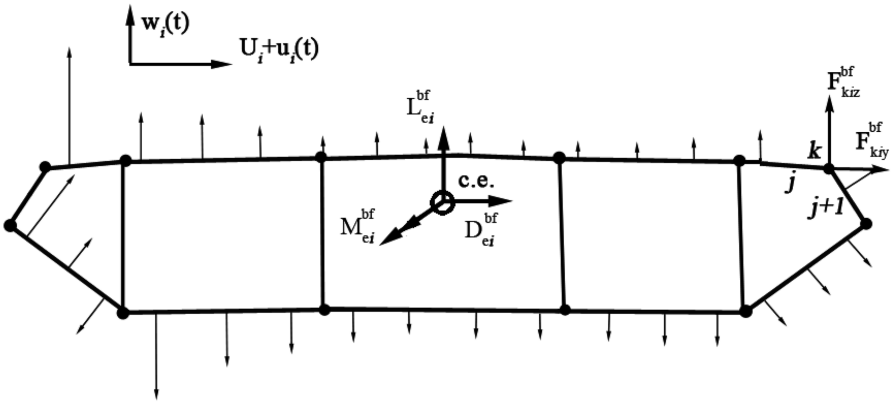

(a) wind pressure distribution

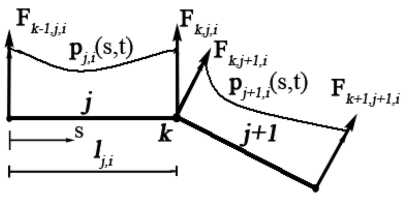

(b) buffeting force at the kth node

Fig. 5 Buffeting wind pressures and buffeting forces at nodes

study. Therefore, an approximate approach based on the matrix $\mathbf{A}_{ei}^{bf}$ in Eq.(3) is proposed here to tackle the problem with the assumption that fluctuating wind pressure distribution over the jth element in the ith deck section can be decomposed as

$$p_{ji}(s,t) = p_{ji}^{m}(s)p_{ji}^{t}(t) \tag{5}$$

where $p_{ji}^{m}(s)$ is the time-invariant part of wind pressure distribution, which may be determined with reference to the mean wind pressure distribution from either wind tunnel tests or computational fluid dynamics (CFD). The time-dependent part $p_{ji}^{t}(t)$ of wind pressure distribution can be related to the fluctuating wind speeds $u_i(t)$ and $w_i(t)$ as

$$p_{ji}^{t}(t) = \begin{bmatrix} B_{uji} & B_{wji} \end{bmatrix} \begin{Bmatrix} u_i(t) \\ w_i(t) \end{Bmatrix} \tag{6}$$

The wind pressure distribution over the entire ith section can then be written as

$$\mathbf{p}_i(s,t) = \begin{bmatrix} p_{1i}^{m}(s) & & 0 \\ & p_{2i}^{m}(s) & \\ & & \cdots \\ 0 & & p_{N_s i}^{m}(s) \end{bmatrix} \mathbf{B}_i \begin{Bmatrix} u_i(t) \\ w_i(t) \end{Bmatrix} \tag{7a}$$

$$\mathbf{B}_i = \begin{bmatrix} B_{u1i} & B_{w1i} \\ B_{u2i} & B_{w2i} \\ \cdots & \cdots \\ B_{uN_s i} & B_{wN_s i} \end{bmatrix} \tag{7b}$$

By introducing only three independent unknown variables in Eq. (7) and comparing with Eq.(3), the three variables can be determined using the following relationships for either the u_i-component or the w_i-component.

$$\sum_{k=1}^{N_d} F_{kiy}^{bf} = D_{ei}^{bf} \tag{8a}$$

$$\sum_{k=1}^{N_d} F_{kiz}^{bf} = L_{ei}^{bf} \tag{8b}$$

$$\sum_{k=1}^{N_d} (F_{kiz}^{bf} h_{ki} - F_{kiy}^{bf} p_{ki}) = M_{ei}^{bf} \tag{8c}$$

in which p_{ki} and h_{ki} are the lateral and vertical coordinates, respectively, of the kth node with respect to the centre of elasticity of the ith deck section. As shown in Fig. 4, the p-axis, h-axis and q-axis originate at the centre of elasticity and are parallel to the directions of y, z and x in the global

coordinate system, respectively. The positive angle α is about the q-axis anticlockwise. It is noted from Eq. (8) that the resultant forces of all the nodal buffeting forces in the ith section are actually equal to the equivalent buffeting forces acting at the centre of elasticity at any given time. This approach therefore ensures that the global bridge responses computed by this approach remain the same as those predicted by the currently-used methods. After the wind pressure distributions over all the sections of the bridge deck are determined by the proposed approach, the buffeting force vector in Eq. (1) can be formed.

3.3. Self-excited forces

The self-excited forces on a bridge deck are due to the interaction between wind and bridge motion. In the time domain, they are often expressed in terms of convolution integrals with impulse response functions (Chen, *et al.* 2000). The self-excited forces acting at the centre of elasticity of the ith deck section can be expressed in the matrix form (Xu, *et al.* 2003).

$$\mathbf{F}_{ei}^{se} = \mathbf{E}_{ei}\mathbf{X}_{ei}(t) + \mathbf{G}_{ei}\dot{\mathbf{X}}_{ei}(t) + \mathbf{H}_{ei}\ddot{\mathbf{X}}_{ei}(t) + \hat{\mathbf{F}}_{ei}^{se} \tag{9}$$

where $\mathbf{F}_{ei}^{se} = \{0, D_{ei}^{se}, L_{ei}^{se}, M_{ei}^{se}, 0, 0\}^T$ is the equivalent self-excited force acting at the centre of elasticity of the ith deck section (see Fig. 6); $\mathbf{X}_{ei}(t)$, $\dot{\mathbf{X}}_{ei}(t)$, $\ddot{\mathbf{X}}_{ei}(t)$ are the displacement, velocity, acceleration vectors, respectively, with respect to the centre of elasticity of the ith section in the p-h-q coordinate system; $\hat{\mathbf{F}}_{ei}^{se}$ is the part of the self-excited forces reflecting aerodynamic phase lag; $\mathbf{E}_{ei}$, $\mathbf{G}_{ei}$ and $\mathbf{H}_{ei}$ are the aeroelastic stiffness, aeroelastic damping and aeroelastic mass matrices, respectively, of the ith deck section with respect to the centre of elasticity. The details of these matrices can be found in the literature (Xu, *et al.* 2003).

Similar to buffeting forces, the actual information on the spatial distribution of self-excited forces over the surface of the ith deck section is not presently available for the purpose of research here. Consequently, to simulate the spatial distribution, the self-excited forces expressed by Eq. (9) with respect to the centre of elasticity of the ith deck section are distributed to the nodal lines of the ith section of the health monitoring-oriented finite element model of the bridge deck. The distributions are based on the rigid body motion relationships between the motions at the nodal lines and those at the centre of elasticity of the ith deck section (Lau, *et al.* 2000). Based on the finite element model of the given ith deck section, the position of the centriod of the ith deck section can be determined in terns of the geometry of the section. The displacement relationship between the nodal lines and the centre of elasticity of the ith section can then be given as follows:

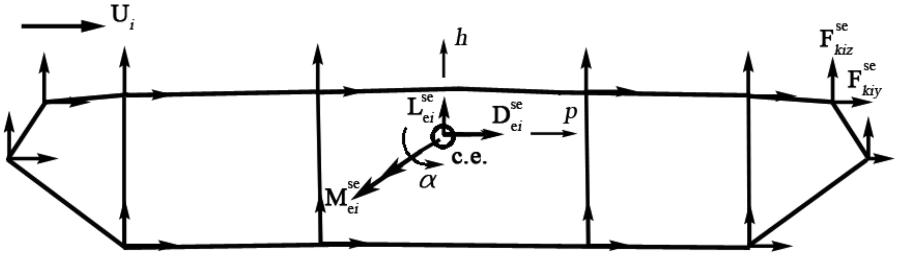

Fig. 6 Self-excited forces at the centre of elasticity and at the nodes in the ith deck section

$$\mathbf{X}_{ei} = \mathbf{N}_i^{se}\mathbf{X}_i \tag{10}$$

where $\mathbf{X}_i = \{\mathbf{X}_{1i}, \mathbf{X}_{2i}, \cdots, \mathbf{X}_{N_di}\}^T$ is the displacement vector of all the nodes in the ith deck section in the *p-h-q* coordinate system; and $\mathbf{N}_i^{se}$ is the displacement transformation matrix which can be expressed as

$$\mathbf{N}_i^{se} = \begin{bmatrix} 0 \\ \mathbf{N}_{Di}^{se} \\ \mathbf{N}_{Li}^{se} \\ \mathbf{N}_{Mi}^{se} \\ 0 \\ 0 \end{bmatrix} \tag{11a}$$

$$\mathbf{N}_{Di}^{se} = \left[0, a_{1i}, h_{ci}b_{1i}, 0, 0, 0, L, 0, a_{N_di}, h_{ci}b_{N_di}, 0, 0, 0\right] \tag{11b}$$

$$\mathbf{N}_{Li}^{se} = \left[0, 0, a_{1i} - p_{ci}b_{1i}, 0, 0, 0, L, 0, 0, a_{N_di} - p_{ci}b_{N_di}, 0, 0, 0\right] \tag{11c}$$

$$\mathbf{N}_{Mi}^{se} = \left[0, 0, b_{1i}, 0, 0, 0, L, 0, 0, b_{N_di}, 0, 0, 0\right] \tag{11d}$$

where h_{ci} and p_{ci} are the vertical and lateral coordinates, respectively, of the centroid of the ith deck section with respect to the *p-h-q* coordinate system; $a_{ki} = \dfrac{\sum_j l_{jki}}{2L_{ci}}$, in which $j = 1,2,\cdots,N_{si}$ and $k = 1, 2,\cdots,N_{di}$, and L_{ci} = the summation of the lengths of all the elements in the ith deck section; $\sum_j l_{jki}$ = the summation of the lengths of all the elements connected at the k th node; and $b_{ki} = \dfrac{1}{N_{di}p_{ki}}$, in which P_{ki} is the lateral coordinate of the kth node in the *p-h-q* coordinate system. The form and the size of the displacement transformation matrix depend on the geometry and discretization of the deck cross section.

The substitution of Eq. (10) into Eq. (9) yields the self-excited forces expressed in terms of the nodal displacements vector for the ith deck section.

$$\mathbf{F}_{ei}^{se} = \mathbf{E}_{ei}\mathbf{N}_i^{se}\mathbf{X}_i + \mathbf{G}_{ei}\mathbf{N}_i^{se}\dot{\mathbf{X}}_i + \mathbf{H}_{ei}\mathbf{N}_i^{se}\ddot{\mathbf{X}} + \hat{\mathbf{F}}_{ei}^{se} \tag{12}$$

By applying the virtual work principle, the self-excited forces at the centre of elasticity of the ith section can be distributed to all of the nodes in the ith section by

$$\mathbf{F}_i^{se} = (\mathbf{N}_i^{se})^T\mathbf{F}_{ei}^{se} = \mathbf{E}_i\mathbf{X}_i + \mathbf{G}\dot{\mathbf{X}}_i + \mathbf{H}\ddot{\mathbf{X}}_i + (\mathbf{N}_i^{se})^T\hat{\mathbf{F}}_{ei}^{se} \tag{13}$$

in which $\mathbf{F}_i^{se} = \{\mathbf{F}_{1i}^{se}, \mathbf{F}_{2i}^{se}, \cdots, \mathbf{F}_{N_d i}^{se}\}^T$ is the nodal self-excited force vector and $\mathbf{F}_{ki}^{se} = \{0, \mathbf{F}_{kiy}^{se}, \mathbf{F}_{kiz}^{se}, 0\ 0, 0\}^T$; $\mathbf{E}_i = (\mathbf{N}_i^{se})^T \mathbf{E}_{ei} \mathbf{N}_i^{se}$, $\mathbf{G}_i = (\mathbf{N}_i^{se})^T \mathbf{G}_{ei} \mathbf{N}_i^{se}$ and $\mathbf{H}_i = (\mathbf{N}_i^{se})^T \mathbf{H}_{ei} \mathbf{N}_i^{se}$ are the aeroelastic stiffness, aeroelastic damping and aeroelastic mass matrices, respectively, of the ith section related to the nodal self-excited forces. By applying the same assembling procedure to all the deck sections, the self-excited force vector in Eq. (1) can be formed accordingly.

$$\mathbf{F}^{se} = \mathbf{E}\mathbf{X} + \mathbf{G}\dot{\mathbf{X}} + \mathbf{H}\ddot{\mathbf{X}} + (\mathbf{N}^{se})^T \hat{\mathbf{F}}^{se} \tag{14}$$

where **E**, **G**, and **H** are the aeroelastic stiffness, aeroelastic damping and aeroelastic mass matrices, respectively, of the bridge related to the nodal self-excited forces in the global coordinate system.

3.4. Determination of bridge responses

The mode superposition technique is adopted in this study to solve Eq. (1) and compute buffeting-induced bridge responses. The nodal displacement vector in Eq. (1) can be expressed by the mode shape matrix and the generalized displacement vector.

$$\mathbf{X}(t) = \mathbf{\Phi}\mathbf{q}(t) \tag{15}$$

where $\mathbf{q}(t) = \{q_1(t), q_2(t), \cdots, q_{N_m}(t)\}^T$ is the generalized displacement vector and N_m is the number of the interested modes involved in the computation; and $\mathbf{\Phi} = [\mathbf{\Phi}_1, \mathbf{\Phi}_2, \cdots, \mathbf{\Phi}_{N_m}]$ is the mode shape matrix with the dimensions $6N \times N_\mathrm{m}$. The equation of motion of wind-excited bridge, that is, Eq. (1) can then be rewritten as

$$\overline{\mathbf{M}}\ddot{\mathbf{q}} + \overline{\mathbf{C}}\dot{\mathbf{q}} + \overline{\mathbf{K}}\mathbf{q} = \mathbf{Q}^{bf} + \mathbf{Q}^{se} \tag{16}$$

in which $\overline{\mathbf{M}}$, $\overline{\mathbf{C}}$ and $\overline{\mathbf{K}}$ are the generalized mass, damping and stiffness matrices, respectively, of the bridge with the dimensions $N_\mathrm{m} \times N_\mathrm{m}$; $\mathbf{Q}^{bf} = \mathbf{\Phi}^T \mathbf{F}^{bf}$ and $\mathbf{Q}^{se} = \mathbf{\Phi}^T \mathbf{F}^{se}$ are the generalized buffeting and self-excited force vectors, respectively.

The substitution of Eq. (14) to Eq. (16) yields

$$(\overline{\mathbf{M}} - \mathbf{\Phi}^T \mathbf{H} \mathbf{\Phi})\ddot{\mathbf{q}} + (\overline{\mathbf{C}} - \mathbf{\Phi}^T \mathbf{G} \mathbf{\Phi})\dot{\mathbf{q}} + (\overline{\mathbf{K}} - \mathbf{\Phi}^T \mathbf{E} \mathbf{\Phi})\mathbf{q} = \mathbf{Q}^{bf} + \hat{\mathbf{Q}}^{se} \tag{17}$$

in which $\hat{\mathbf{Q}}^{se} = \mathbf{\Phi}^T (\mathbf{N}^{se})^T \hat{\mathbf{F}}^{se}$.

It is convenient to normalize the modal matrix to satisfy the following orthogonal condition.

$$\mathbf{\Phi}^T \mathbf{M} \mathbf{\Phi} = \mathbf{I}, \quad \mathbf{\Phi}^T \mathbf{K} \mathbf{\Phi} = \mathrm{diag}\left[\omega_1^2, \omega_2^2, \cdots, \omega_{N_m}^2\right] \tag{18}$$

The generalized mass matrix is then the unit matrix $\overline{\mathbf{M}} = \mathbf{I}$. The generalized stiffness matrix is obtained by the natural frequencies only, namely, $\overline{\mathbf{K}} = \mathrm{diag}[\omega_1^2, \omega_2^2, \cdots, \omega_{N_m}^2]$ where ω_i is the ith circular natural frequency of the bridge structure. The generalized damping matrix is expressed in the form of modal viscous damping ratios, that is, $\overline{\mathbf{C}} = \mathrm{diag}[2\zeta_1\omega_1, 2\zeta_2\omega_2, \cdots, 2\zeta_{N_m}\omega_{N_m}]$ where ζ_i is the ith modal damping ratio of the bridge structure. The generalized displacement vector $\mathbf{q}(t)$ in Eq. (17) can be solved using the Newmark implicit integral algorithm. The nodal displacement,

velocity, and acceleration vectors can then be determined based on Eq. (15).

Once the nodal displacement vector is determined, the element stress induced by the elastic deformation of the jth element without considering initial strains and stresses can be computed by

$$\boldsymbol{\sigma}_j = \mathbf{D}_j\mathbf{L}_j\mathbf{N}_j\mathbf{X}_j \tag{19}$$

in which $\boldsymbol{\sigma}_j$ is the jth element stress vector, namely, $\boldsymbol{\sigma}_j = \{\sigma_x, \sigma_y, \sigma_z, \tau_{xy}, \tau_{yz}, \tau_{zx}\}_j^T$; $\mathbf{X}_j$ is the nodal displacement vector of the jth element; $\mathbf{N}_j$ is the shape function of the jth element; $\mathbf{L}_j$ is the differential operator that can transfer the displacement field to the strain field; and $\mathbf{D}_j$ is the elastic matrix which establishes the relationship between the stress and the strain of the jth element. The modal stresses of all the elements at their end sections in the global coordinate system can be derived from the following relationship:

$$\Gamma = \mathbf{DLN}\Phi \tag{20}$$

where **D**, **L** and **N** are the elastic matrix, the differential operator and the shape function, respectively, of the bridge structure in the global coordinate system. With the introduction of the modal stresses, the stresses of the element can be obtained from the superposition of the modal stresses with the generalized displacements.

4. Field measurement data from WASHMS

The framework for buffeting-induced stress analysis using the structural health monitoring oriented finite element model of Tsing Ma Bridge established here should be verified before it can be used in practice. The verification of the framework is based on the field measurement data recorded by a wind and structural health monitoring system (WASHMS) installed in the Tsing Ma Bridge by the Hong Kong Highways Department (Wong 2004). It has been more than ten years since Tsing Ma Bridge was opened to the public in 1997. However, only on September 16, 1999, during Typhoon York, which was the strongest typhoon since 1983 and the typhoon of the longest duration on record in Hong Kong, all vehicles except trains were prohibited from running on the bridge. This event provides a distinctive opportunity to examine the proposed procedure for buffeting-induced stress analysis of long suspension bridges. Wind data from the anemometers, bridge deck acceleration responses from the accelerometers, and bridge deck stress responses from the strain gauges recorded by the WASHMS, as shown in Fig. 7, during this event are therefore analyzed subsequently.

4.1. Wind characteristics

On September 12, 1999, the tropical depression York developed at about 430 km northeast of Manila and intensified into a tropical storm on the next day over the South China Sea (HKO 1999). After moving northwest for almost two days, Typhoon York passed Hong Kong on the early morning of September 16. Signal No.10 was forced to hoist for 11 hours, the longest on record in Hong Kong. All vehicles except trains were prohibited from running on Tsing Ma Bridge for two and a half hours from 3:30 p.m. to 6:00 p.m. on September 16, 1999.

Wind data of 2.5h duration recorded by the anemometer at the top of the Tsing Yi tower were

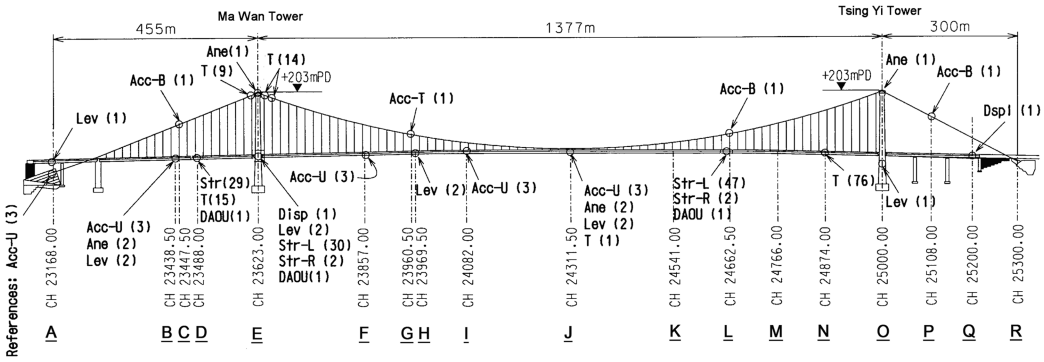

Fig. 7 The layout of sensory system in Tsing Ma Bridge

analyzed first. The wind data were evenly divided into segments of 3-minute long each with 1.5-minute overlap between neighboring segments. The duration of 3 minutes was chosen based on the fact that it takes about 1.5 to 2.0 minutes for a train to completely pass through the whole bridge and the fact that some anemometers at the deck level were out of order during Typhoon York. For each data segment, the mean wind direction was determined, by which wind data recorded by the two ultrasonic anemometers (WI-TJN-01 and WI-TJS-01) at the deck level in the main span were selected with the principle that the anemometer selected should directly face the incident wind and the wind data selected were not contaminated due to the bridge deck itself. For all wind data segments selected, the mean wind direction at the deck level was calculated. The data segments with wind direction perpendicular to the bridge alignment (with a tolerance of $\pm 14^{o}$) were then taken as qualified data segments. The qualified data segments without trains running on the bridge within the duration of wind data segments were finally selected. Displayed in Fig. 8 are the 3 minute time histories of fluctuating wind components in alongwind and upward directions for the case, where there was no train passing through the bridge and the bridge was subjected to mainly high cross winds, used in this study. The mean wind speed, mean wind direction, mean wind incidence, alongwind turbulence intensity, and upward turbulence intensity corresponding to the wind time histories shown in Fig. 8 are 18.8 m/s, -1.4^{o}, 3.5^{o}, 10.3% and 7.3%, respectively. Since the mean wind direction refers to the axis perpendicular to the bridge alignment, the mean wind direction of the selected data segment is almost perpendicular to the bridge alignment so as to

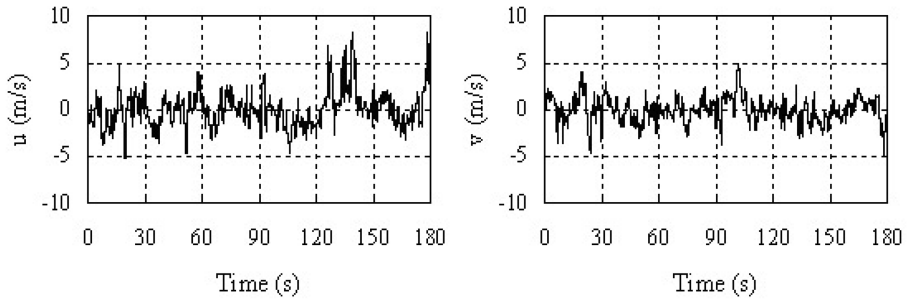

(a) along wind (b) upward wind

Fig. 8 Time histories of measured fluctuating wind components

facilitate the comparison between the measured and computed bridge responses.

To obtain wind auto spectrum, the Fast Fourier Transform (FFT) technique was used, and 3 minutes time history was re-sampled at 51.2 Hz and then divided into 4 sub-segments with a properly overlapped length so that each segment contains 4096 data points. The frequency resolution in the spectral analysis was 0.0125 Hz. Furthermore, the piecewise smoothing method and the hamming window were adopted in the spectral analysis. The wind auto spectra were fitted using non-linear least squares method with the following objective function.

$$n_f S_j(n_f) = \frac{n_f a}{(1 + b n_f^{1/m})} (m^2/s) \tag{21}$$

where the subscript j of S can be u or w (along wind and upward wind); c is a constant exponent using 5/3; n_f is the frequency of wind turbulence in Hz; and a, b and m are the parameters to be fitted. For the concerned two time histories, the fitted parameters a, b and m are, respectively, 81.11, 7.29 and 1.43 for the alongwind spectrum and 10.17, 60.69, and 0.54 for the upward spectrum. The fitted auto spectra together with other wind characteristics will be used for the numerical simulation of the stochastic wind speed field for the whole bridge deck.

4.2. Measured acceleration responses of bridge deck

The first 80 modes of vibration of the bridge are included in the numerical computation of bridge deck acceleration and stress responses. The highest frequency in the computed acceleration response is about 1.1 Hz. To have a reasonable comparison between the measured and computed buffeting responses, the measured acceleration time histories should go through a digital low pass filter with the upper bound of frequency 1.1 Hz. Time histories of one lateral and two vertical acceleration responses of the bridge deck at each of the four sections (Section B, F, I, J in Fig. 7) corresponding to the 3 minute wind time histories were processed. Fig. 9 shows the positions of two vertical accelerometers, horizontally separated by 26 m, measuring accelerations in the vertical direction and one lateral accelerometer measuring acceleration in the lateral direction. The maximum and root mean square (RMS) acceleration responses were calculated and the results are listed in Table 1 to compare with the computed ones. In Table 1, Section B is located in the Ma Wan side span, whereas Sections F, I and J are located at 1/6, 1/3 and 1/2 of the main span, respectively.

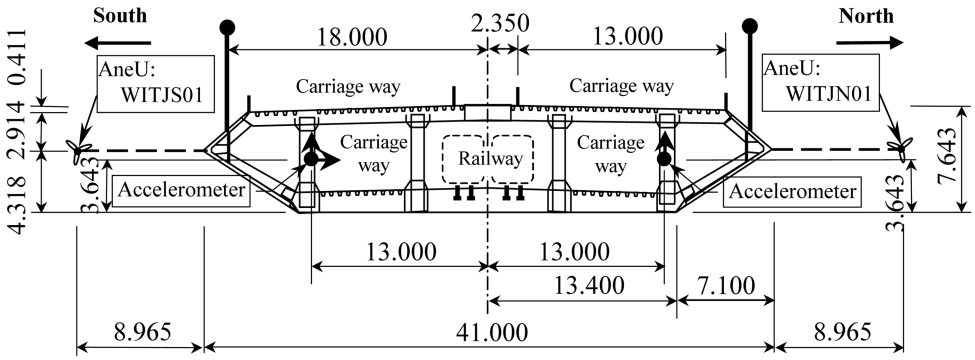

Fig. 9 Positions of three accelerometers in the deck cross section

Table 1 Measured and computed acceleration responses of bridge deck

Lateral acceleration							
Cross section	Tag No. of accelerometer	RMS (mm/s^2)			Maximum (mm/s^2)		
		Measured	Computed	RD*(%)	Measured	Computed	RD(%)
B	AT-TBS-01	17.47	16.56	5.20	49.88	52.38	-5.01
F	AT-TFS-01	9.16	10.43	-13.93	24.49	38.57	-57.49
I	AT-TIS-01	10.03	10.41	-3.80	30.76	35.32	-14.81
J	AT-TJS-01	10.56	11.67	11.68	31.91	41.53	-30.16
Vertical acceleration							
Cross section	Tag No. of accelerometer	RMS (mm/s^2)			Maximum (mm/s^2)		
		Measured	Computed	RD(%)	Measured	Computed	RD(%)
B	AT-TBS-01	70.77	51.56	27.14	224.73	194.64	13.39
	AT-TBN-01	69.46	50.12	27.84	193.76	162.90	15.93
F	AT-TFS-01	61.84	62.86	-1.66	205.01	206.63	-0.79
	AT-TFN-01	66.22	64.31	2.88	206.41	254.50	-23.30
I	AT-TIS-01	63.67	71.39	-12.13	182.64	258.55	-41.56
	AT-TIN-01	65.78	67.07	-1.96	211.41	260.95	-23.43
J	AT-TJS-01	69.35	72.33	-4.29	216.76	229.70	-5.97
	AT-TJN-01	69.84	76.31	-9.27	250.94	227.94	9.17

*RD: Relative Difference

4.3. Measured stresses of bridge deck

For the purpose of comparison with the computed results, 10 strain gauges arranged on the longitudinal trusses of the bridge deck at Section L were selected. Section L is located at almost 3/4 of the main span form the Ma Wan tower side. The tag number and location detail of each strain gauge can be found in Table 2 and Fig. 10. The strain gauges with the tag numbers “SS-

Table 2 Tag number and location details of 10 strain gauges used in this study

Tag No. of Strain Gauge	Location Details	Element Number
SP-TLN-01	North truss top chord	31341
SS-TLN-01	North truss top chord	
SP-TLN-05	North truss bottom chord	32341
SS-TLN-03	North truss bottom chord	
SP-TLS-12	South truss bottom chord	36341
SS-TLS-09	South truss bottom chord	
SP-TLN-02	North truss diagonal	32341
SP-TLN-03	North truss diagonal	32342
SP-TLS-02	South truss diagonal	36341
SP-TLS-03	South truss diagonal	36342

TLN-xx" and "SS-TLS-xx" are the single linear strain gauge arranged on the north and south longitudinal trusses of Section L, respectively. The tag numbers "SP-TLN-xx" and "SP-TLS-xx" represent a pair of linear strain gauges arranged on the north and south longitudinal trusses of Section L, respectively, with one single output. It can be noted that the selected strains are all located at the middle of the elements to avoid the effect of stress concentration and to facilitate

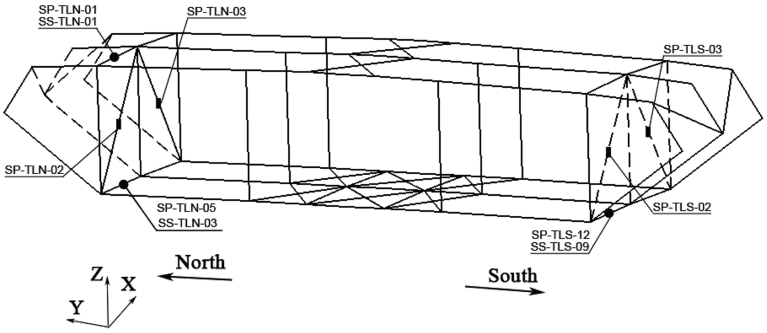

(a) global positions

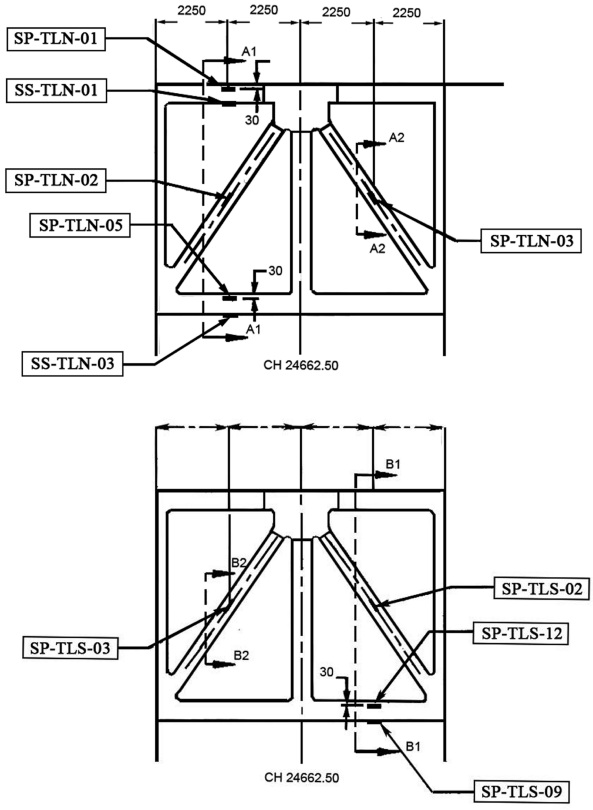

(b) positions in longitudinal trusses

Fig. 10 Locations of 10 strain gauges used in this study

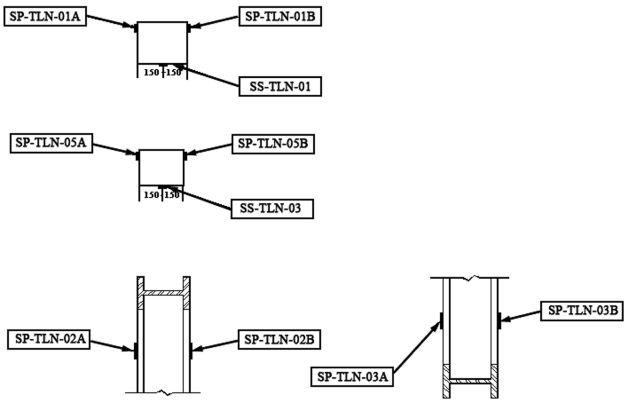

(c) local positions

Fig. 10 Continued

Table 3 Measured and computed stress responses of bridge deck

Tag No. of Strain Gauge	RMS (MPa)			Maximum (MPa)		
	Measured	Computed	RD(%)	Measured	Computed	RD (%)
SP-TLN-01	1.4824	0.9909	33.15	5.1765	3.7662	27.24
SS-TLN-01	1.4246	0.8895	37.56	4.7470	3.3586	29.25
SP-TLN-05	1.7117	1.1068	35.34	4.8009	3.4796	27.52
SS-TLN-03	1.9424	1.4428	25.72	5.2498	4.0755	22.37
SP-TLS-12	1.6625	1.2157	26.88	5.8009	4.7426	18.24
SS-TLS-09	1.8363	1.5844	13.72	6.3699	5.8040	8.88
SP-TLN-02	1.4489	1.4354	0.93	4.0886	4.4693	-9.31
SP-TLN-03	1.4083	1.4270	-1.33	3.9745	4.4464	-11.87
SP-TLS-02	1.3889	1.3107	5.63	4.1517	4.2061	-1.31
SP-TLS-03	1.4190	1.3080	7.82	4.3249	4.0949	5.32

the comparison. The measured strain was converted to the measured stress by multiplying the modulus of elasticity for steel material $E = 2.05\times10^{11}$ N/m^2. The stress time histories then go through a digital low pass filter with the upper bound of frequency 1.1 Hz to be compatible with the highest frequency involved in the computation results. The time histories of the 10 stress responses of the bridge deck at Section L corresponding to the 3 minute wind time histories were further processed to remove the mean stresses. The maximum and root mean square (RMS) stress responses were then calculated and the results are listed in Table 3 for comparison with the computed ones.

5. Numerical results and comparison

It is necessary to verify the proposed stress analysis procedure through comparison with field

measurement data. The wind characteristics obtained from the measured wind data together with other information are used for the digital simulation of stochastic wind velocity field around the bridge. The simulated wind velocity field is then used to generate buffeting forces at the nodes as input parameters, together with self-excited forces at the nodes, to the structural health monitoring oriented finite element model of Tsing Ma Bridge to predict bridge responses The computed acceleration and stress responses of the bridge deck are finally compared with the measured acceleration and stress responses to verify the proposed approach to some extent.

5.1. Wind field simulation

Since fluctuating wind pressure distribution over the deck surface of the Tsing Ma Bridge is not available, the approximate approach proposed in Section 3.2 of this paper is used to estimate buffeting forces at the nodes of the FEM of the bridge. In this regard, a series of time histories of fluctuating wind velocity in horizontal and vertical directions at various points along the bridge deck is essential. However, there were only two anemometers installed along the bridge deck on each side. This situation was further worsened for the bridge subjected to Typhoon York because during Typhoon York, the anemometers installed at deck level were out of order for a certain period. Therefore, in this study the horizontal and vertical wind auto-spectra, the mean wind speed, the mean wind incidence, and the turbulent intensities obtained from the measured wind velocities at the mid-main span of the bridge deck (see Section 4.1 of this paper) are assumed to be constant along the bridge deck. The exponential form of coherence function is adopted to reflect turbulent wind correlation along the bridge deck in both the horizontal and vertical directions. The exponential decay coefficient is selected as 16 in the simulation (Simiu and Scanlan 1996). A fast spectral representation approach proposed by Cao, *et al.* (2000) is then adopted here for the digital simulation of stochastic wind velocity field. A total of 120 points along the bridge with an interval 18.0 m are considered in the simulation of wind field. The average elevation of the bridge deck is taken as 60 m. The sampling frequency and duration used in the simulation of wind speeds are, respectively, 50 Hz and 10 minutes. The use of 10 minutes duration rather than 3 minutes duration is to consider the proper simulation of dynamic interaction between wind and bridge. The corresponding frequency interval and the time interval of wind velocity are 0.0015Hz and 0.02s respectively. Fig. 11 illustrates the simulated turbulent wind velocity time-histories of 10 minutes duration in the alongwind (horizontal) and upward (vertical) directions at the mid-main span of the bridge deck.

5.2. Buffeting forces and self excited forces

Since actual fluctuating wind pressure distribution over the deck surface of the Tsing Ma Bridge is not known, the approximate approach proposed in Section 3.2 of this paper is used to estimate buffeting forces at the nodes of the FEM of the bridge. With reference to the mean wind pressure distributions on the typical deck sections of Tsing Ma Bridge, the time-invariant part of wind pressure distribution over the three typical deck sections is decided and shown in Fig. 12. The three typical deck sections have 12, 10 and 8 nodes, respectively. It can be seen from Fig. 12 that the time-invariant part of wind pressure distribution over each deck section contains three independent variables p_1, p_2 and p_3. The three variables can be determined using Eq.(8) for the u_i-component and the w_i-component separately. In the determination of the three variables, the drag, lift, and moment

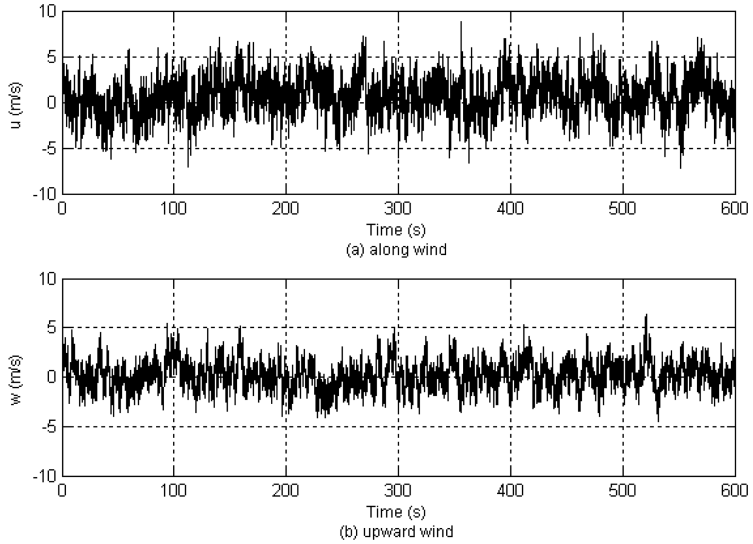

Fig. 11 Time histories of simulated fluctuating wind components at midmain span

coefficients of the bridge deck of 12-node section measured from wind tunnel tests are 0.104, 0.210, and 0.082, respectively, at the wind angle of attack of 3.5° with respect to the deck width of 41 m (Xu, *et al.* 2000). The first derivatives of the drag, lift, and moment coefficients with respect to the same wind angle of attack are -0.172, 1.719, and 0.344, respectively. The aerodynamic coefficients for the other two deck sections are not available so that the aerodynamic coefficients for the 12-node section are applied to the other two deck sections. The aerodynamic transfer functions between fluctuating wind velocities and buffeting forces in Eq. (3) are assumed to be one. After the wind pressure distributions over all the sections of the bridge deck are determined, the buffeting force vector in Eq. (1) can be formed according to the procedure mentioned in Section 3.2 of this paper.

To determine the self-excited forces at the nodes of the FEM of the Tsing Ma Bridge, the aeroelastic stiffness matrix and the aeroelastic damping matrix of the typical deck section with respect to the centre of elasticity in Eq. (9) shall be determined first. The aerodynamic mass matrix in Eq. (9) is normally neglected in practice. The number of terms used in $\hat{\mathbf{F}}_{ei}^{se}$ of Eq. (9) is normally set as 2. Due to the lack of wind tunnel test results on lateral flutter derivatives, only the vertical and rotational motions of the bridge deck are taken into account in the simulation of self-excited forces. Moreover, the coupled terms are neglected since they have smaller effects on the self-excited forces. As a result, a total of 12 frequency independent coefficients are determined by using the measured flutter derivatives and the least squares fitting method, and they are used to determine the matrices $\mathbf{E}_{ei}$ and $\mathbf{G}_{ei}$ and the coefficients in the vector $\hat{\mathbf{F}}_{ei}^{se}$ for the ith typical deck section. Because of the geometrical symmetry with respect to the mid-vertical axis of the bridge deck section, the centre of elasticity and the centroid of the deck cross section both are in the vertical axis. By taking this geometric feature into account, the displacement transformation matrix $\mathbf{N}_i^{se}$ in Eq. (10) for the ith typical deck section can be determined easily. The aeroelastic stiffness matrix $\mathbf{E}$, the aeroelastic damping matrix $\mathbf{G}$, the coefficients in the vector $\hat{\mathbf{F}}^{se}$, and the self-excited forces at the nodes of the FEM of the Tsing Ma Bridge in the global coordinate system can then be determined using Eqs.(13) and (14).

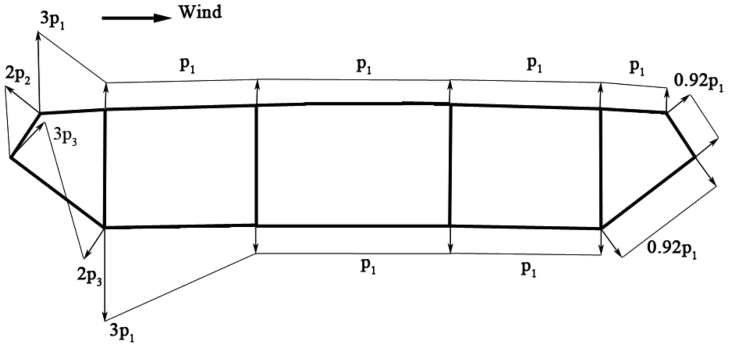

(a) 12-node section

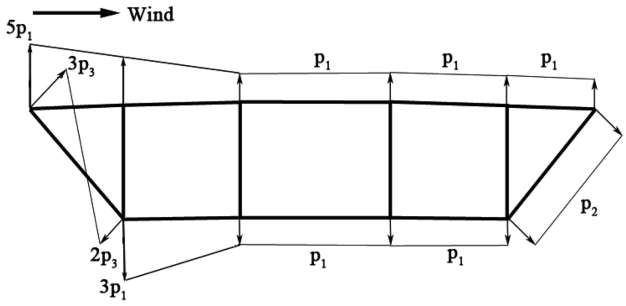

(b) 10-node section

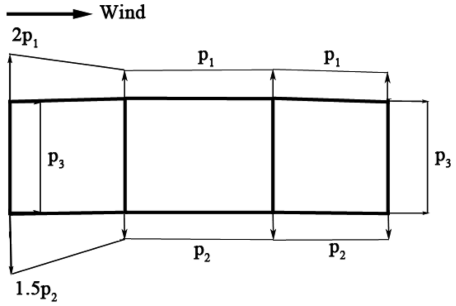

(c) 8-node section

Fig. 12 Time-invariant part of wind pressure distribution over three typical deck sections

5.3. Comparison of bridge acceleration responses

The buffeting-induced acceleration and stress responses of Tsing Ma Bridge are computed using the mode superposition technique as discussed in Section 3.4 of this paper. The first 80 modes of vibration of the Tsing Ma Bridge are considered in the computation. The highest frequency involved in the computation is 1.1 Hz. The damping ratios for all the modes of vibration are taken as 0.5%. The generalized displacement vector $\mathbf{q}(t)$ in Eq. (17) is solved using the Newmark implicit integral algorithm with $\beta = 0.25$. The nodal displacement, velocity, and acceleration vectors are determined based on Eq. (15). The number of time steps used in the computation is 2^{15} with a time interval of 0.02s. This is the same as that used in the simulation of wind velocity field.

The acceleration responses are computed for all the nodes of the FEM of the Tsing Ma Bridge.

Some of them are then converted to the acceleration responses at the locations of accelerometers through the shape function of the element for comparison. Fig. 13 illustrates the computed and

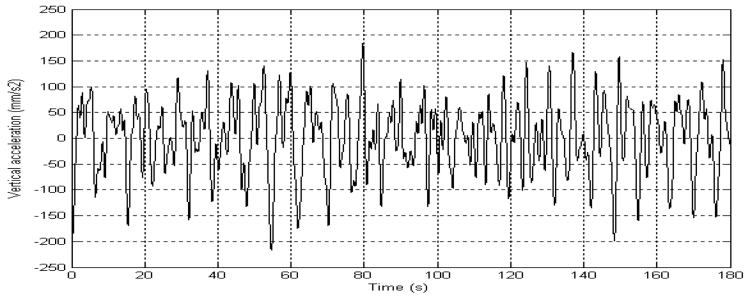

(a) measured vertical acceleration

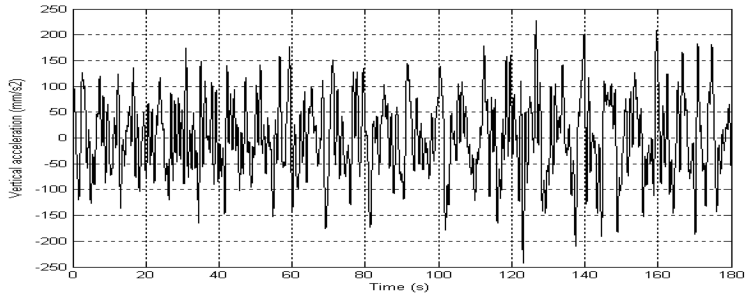

(b) computed vertical acceleration

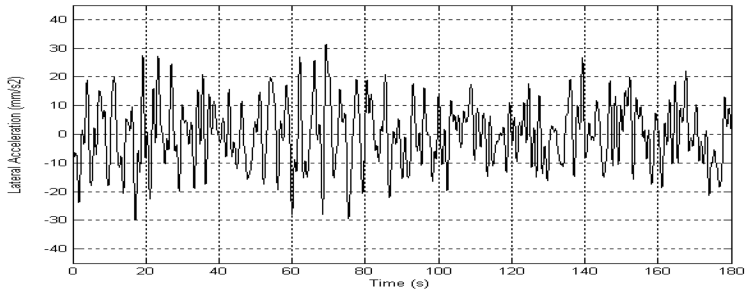

(c) measure lateral acceleration

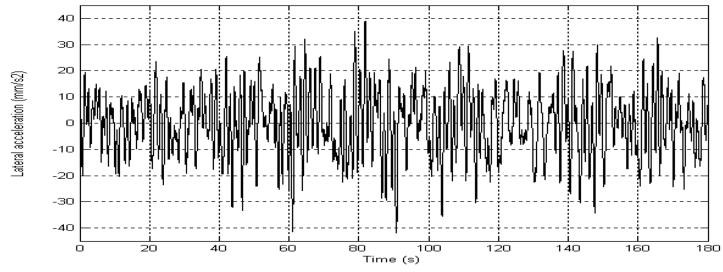

(d) computed lateral acceleration

Fig. 13 Computed and measured acceleration response time histories of 3 minutes duration (Section J, South)

measured acceleration response time histories of 3 minutes duration for Section J of the bridge deck in the vertical direction and the lateral direction on south side. The computed and measured maximum accelerations and RMS accelerations are listed in Table 1 together with the relative differences (RD: the measured one minus the computed one and then divided by the measured one) for the two vertical points and one lateral point in each of the four sections (Sections B, F, I and J) where the accelerometers were installed. It can be seen from Fig. 13 that the computed vertical and lateral acceleration time histories are similar in both pattern and magnitude with the measured ones. Since the time period of the computed time histories does not coincide with that of the measured ones so that the exact comparison is impossible. It can be seen from Table 1 that for lateral accelerations, the computed RMS accelerations are closer to the measured ones than the computed maximum accelerations for the four deck sections concerned. The relative differences in the RMS lateral accelerations range from 5.2% to 13.93%. The relative differences in the maximum lateral accelerations range from 5.01% to 57.49%. Similar observations are made for the vertical acceleration responses. The relative differences in the RMS vertical accelerations range from 1.66% to 27.84% whereas those in the maximum vertical accelerations range from 0.79% to 41.56%. The relatively large difference in the maximum acceleration responses is due to the relatively short time period of the measured data available. The further comparison using the long period of measured data is desirable in the future.

5.4. Comparison of bridge stress responses

The 10 strains gauges concerned in this study are actually arranged in 7 elements as listed in Table 2. The 4 strain gauges (SP-TLN-02, SP-TLN-03, SP-TLS-02 and SP-TLS-03) are stuck on and along the neutral axis of the diagonal elements as shown in Fig. 10, and therefore these stresses are caused by the axial forces only. The other 6 strain gauges are stuck on either the top or bottom surface of the truss chords. These stresses are caused by both the bending moments and the axial forces. To compare with the measured stresses at the locations of 9 strain gauges, the modal stresses of the relevant 7 elements at their end sections are computed according to Eq.(20) using the commercial computer program. The modal stresses are then multiplied by the generalized displacement vector to yield the stress time histories at 5 points of the end section of each element. Among 5 points, 4 points are located at each corner of the end section and 1 point is situated at the centroid of the end section. For the 4 diagonal elements (see Fig. 10), the stress time history at the centriod of the end section is taken as the stress time history at the location of the strain gauge. For the truss chords, the stress time histories at the corners of the two end sections are properly combined to give the stress time history at the location of the strain gauge. Fig. 14 illustrates the computed and measured stress response time histories of 3 minutes duration at the location of strain gauge SP-TLN-01. The computed and measured maximum stresses and RMS stresses are listed in Table 3 together with the relative differences (RD) for the 10 strain gauges concerned. It can be seen from Fig. 14 that the computed stress time history is similar with the measured one. Since the time period of the computed time history does not coincide with that of the measured one so that the exact comparison is impossible again. It can be seen from Table 3 that the computed RMS and maximum stresses on the four diagonal elements (SP-TLN-02, SP-TLN-03, SP-TLS-02 and SP-TLS-03) are in good agreement with the measured ones. The relative differences in the RMS stress range from 0.93% to 7.82%. The relative differences in the maximum stress range from 1.31% to 11.87%. Nevertheless, the computed RMS and maximum stresses on the truss chords are not so well comparable with the

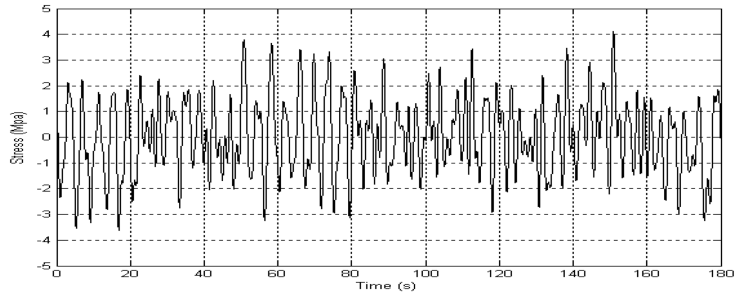

(a) measured stress response

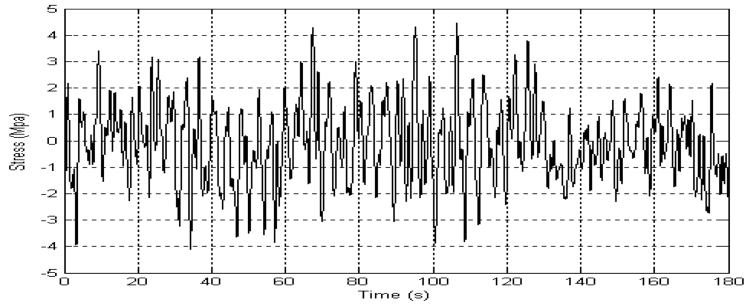

(b) computed stress response

Fig. 14 Computed and measured stress response time histories of 3 minutes duration (SP-TLN-01)

measured ones. The relative differences in the RMS stress range from 13.72% to 37.56% whereas those in the maximum stress range from 8.88% to 29.25%. The relatively large difference in the chord stress comparison is attributed to the complex connections between the chords of the longitudinal trusses and the orthotropic deck plates. The accurate modelling of stiffened deck plates is very complicated and not fulfilled in this study.

6. Conclusions

This paper has presented a structural health monitoring (SHM) oriented finite element model (FEM) and a numerical procedure for buffeting induced stress analysis of a long suspension bridge. The approximate approach to determine buffeting forces and self-excited forces at the nodes of SHM-FEM of the bridge deck has been presented. The field measurement data including wind, accelerations and stresses recorded by the wind and structural health monitoring system (WASHMS) installed on the Tsing Ma Bridge during Typhoon York in 1999 have been analyzed and used to verify the proposed numerical procedure.

The buffeting–induced acceleration responses at the locations of 12 accelerometers installed in the Tsing Ma Bridge has been computed using the mode superposition method and compared with the measured results. The buffeting-induced stress responses at the locations of 9 strain gauges installed in the bridge have been computed through the modal stress analysis and compared with the measured ones. The comparative results show that the computed acceleration and stress time

histories are similar with the measured ones. The computed RMS accelerations are closer to the measured ones than the computed maximum accelerations for the four deck sections concerned. The computed RMS and maximum stresses on the four diagonal elements are in good agreement with the measured ones. Nevertheless, the computed RMS and maximum stresses on the truss chords are not so well comparable with the measured ones because of the complex connections between the chords of the longitudinal trusses and the orthotropic deck plates in reality.

It is worthwhile to point out that the comparative study presented in this paper is just for one single event. This is obviously insufficient for the verification of the proposed numerical procedure for SHM oriented stress analysis. Moreover, the information on the spatial distribution of buffeting-induced wind pressure over a deck surface is very limited. Therefore, further investigation on these topics and more comparative studies are needed in the future before solid conclusions can be reached.

Acknowledgements

The authors are grateful to the financial support from the Research Grants Council of Hong Kong through the competitive research grant (PolyU 5327/08E). The support from the Highways Department of HKSAR for providing the field measurement data is greatly appreciated. All views expressed in this paper are entirely those of the authors.

References

Cao, Y.D., Xiang, H.F. and Zhou, Y. (2000), "Simulation of stochastic wind velocity field on long-span bridges", *J. Eng. Mech.* ASCE, **126**(1), 1-6.

Chan, T.H.T., Zhou, T.Q., Li, Z.X. and Guo, L. (2005), "Hot spot stress approach for Tsing Ma Bridge fatigue evaluation under traffic using finite element method", *Struct. Eng. Mech.*, **19**(3), 261-279.

Chen, X.Z., Matsumoto, M. and Kareem, A. (2000), "Time domain flutter and buffeting response analysis of bridges", *J. Struct. Eng.* ASCE, **126**(1), 7-16.

Davenport, A.G. (1962), "Buffeting of a suspension bridge by storm winds", *J. Struct. Div.* ASCE, **88**, 233-268.

HKO (1999), Typhoon York (9915): 12-17 September 1999, Hong Kong Observatory, (http://www.info.gov.hk/hko/informtc/tork/report.htm), Sept. 1999.

Jain, A., Jones, N.P. and Scanlan, R.H. (1996), "Coupled flutter and buffeting analysis of long-span bridges", *J. Struct. Eng.* ASCE, **122**(7), 716-725.

Lau, D.T., Cheung, M.S. and Cheng, S.H. (2000), "3D flutter analysis of bridges by spline finite-strip method", *J. Struct. Eng*. ASCE, **126**(10), 1246-1254.

Li, X.Z., Chan, T.H.T. and Ko, J.M. (2002), "Evaluation of typhoon induced damage for Tsing Ma Bridge", *Eng. Struct*., **24**, 1035-1047.

Lin, Y.K. and Yang, J.N. (1983), "Multimode bridge response to wind excitations", *J. Eng. Mech.* ASCE, **109**, 586-603.

Liu, G., Xu, Y.L. and Zhu, L.D. (2004), "Time domain buffeting analysis of long suspension bridges under skew winds", *Wind Struct*., **7**(6), 421-447.

Scanlan, R.H. and Gade, R.H. (1977), "Motion of suspension bridge spans under gusty wind", *J. Struct. Div.* ASCE, **103**, 1867-1883.

Simiu, E. and Scanlan, R.H. (1996), *Wind Effects on Structures*, Wiley, New York.

Wong, K.Y. (2002), *Structural identification of Tsing Ma Bridge*, The Hong Kong Institution of Engineers, **10**(1), 38-47.

Wong, K.Y. (2004), "Instrumentation and health monitoring of cable-supported bridges", *J. Struct. Control*

Health Monit., **11**, 91-124.
Xu, Y.L., Ko, J.M. and Zhang, W.S. (1997), "Vibration studies of Tsing Ma long suspension bridge", *J. Bridge Eng.* ASCE, **2**(4), 149-156.
Xu, Y.L., Sun, D.K., Ko, J.M. and Lin, J.H. (2000), "Fully coupled buffeting analysis of Tsing Ma suspension bridge", *J. Wind Eng. Ind. Aerod*., **85**, 97-117.
Xu, Y.L., Xia, H. and Yan, Q.S. (2003), "Dynamic response of suspension bridge to high wind and running train", *J. Bridge Eng*. ASCE, **8**(1), 46-55.
Zhang, W.S., Wong, K.Y., Xu, Y.L., Liu, T.T., Zhou, H.J. and Chan, K.W.Y. (2007), "Buffeting-induced Stresses in a Long Suspension Bridge: Structural Health Monitoring Oriented Finite Element Model", Research Report, Department of Civil and Structural Engineering, The Hong Kong Polytechnic University.

CC